Energy Reports 13 (2025) 105–116

Contents lists available at ScienceDirect

Energy Reports

journal homepage: www.elsevier.com/locate/egyr

Research Paper

Optimizing all-solid-state sodium-ion batteries: Insights from a P2D Model on NaSICON-based polymer–ceramic electrolyte

F. Gerbig *, J. Kühn, H. Nirschl

Institute of Mechanical Process Engineering and Mechanics, Karlsruhe Institute of Technology (KIT), Straße am Forum 8, 76131 Karlsruhe, Germany

ARTICLE INFO

Keywords:
All-solid-state battery
Computational modeling
Sodium battery
Polymer–ceramic electrolytes
Sustainable energy storage
Battery design optimization
Sodium
Energy conversion

ABSTRACT

Rechargeable batteries are integral to modern technology, with lithium-ion batteries (LIBs) leading in portable electronics and electric vehicles. However, the abundance and global distribution of sodium have renewed interest in sodium-ion batteries (SIBs) as a sustainable alternative, particularly for stationary energy storage and applications with less stringent energy density needs. This study develops a pseudo-two-dimensional (P2D) model to investigate the performance of all-solid-state sodium-ion batteries (ASSSIBs) with hybrid polymer–ceramic electrolytes. We compare this model with a particle-resolved microstructure model to derive effective transport parameters. Our results highlight the significance of electrolyte composition and cell design to mitigate transport limitation in the electrolyte and maximize battery performance. Optimal cell design varies with C-rate, requiring lower active material fractions and more uneven particle distributions for higher rates. Optimization shows that the charge process can harness more cell capacity than discharging, suggesting a bottleneck in the discharge process. These insights guide the development of more efficient and reliable ASSSIBs, emphasizing the importance of fast-ion conducting solid electrolytes for future advancements.

1. Introduction

Rechargeable batteries are pivotal to modern technological advancements due to their scalability, cost-efficiency, and significant energy storage capabilities (Jin et al., 2020). Lithium-ion batteries (LIBs) have achieved substantial commercial success, particularly in portable electronics and electric vehicles, due to their high energy density and long lifespan (Delmas, 2018). However, the reliance on critical materials like lithium and cobalt, coupled with the rising cost and environmental impact of their extraction, has driven research into alternatives such as sodium-ion batteries (SIBs) (Nayak et al., 2018).

Sodium is an abundant, globally distributed element, making SIBs a promising alternative for applications like stationary energy storage and small vehicles, where lower energy density requirements are acceptable (Delmas, 2018). Furthermore, SIBs enable the use of abundant cathode materials like iron, manganese, and copper, reducing reliance on critical elements such as cobalt and nickel used in LIBs (Titirici et al., 2022). Despite these advantages, SIBs face unique challenges due to the larger size and weight of sodium ions, which lead to poor phase stability, slower ion transport kinetics, and unfavorable interphase formation in host materials (Liu et al., 2022; Usiskin et al., 2021; Fan and Li, 2018).

The electrolyte plays a central role in determining the performance of SIBs by facilitating Na^+ transport between the cathode and the anode. Conventional liquid electrolytes, while offering high ionic conductivity, suffer from poor electrochemical and thermal stability and promote dendrite formation in sodium metal anodes, limiting cycle life and safety (Li et al., 2023; Fan and Li, 2018). In contrast, solid-state electrolytes eliminate many of these issues by replacing liquid components with solid alternatives like polymers, inorganic ceramics, glassy phases, or hybrid systems (Liu et al., 2023; Eshetu et al., 2020; Dong et al., 2024). Among these, hybrid polymer–ceramic electrolytes, combining the mechanical flexibility of polymers with the high ionic conductivity of ceramics, offer a balance between performance and manufacturability (Zou et al., 2020).

Within this category, NaSICON-type materials stand out as active ceramic fillers due to their high ionic conductivity, chemical stability, and sustainability, as they do not rely on critical elements (Zhang et al., 2016; Chen et al., 2019). Recent research has explored their use in hybrid electrolytes to enhance sodium-ion transport, reduce contact resistance, and enable compatibility with sodium metal anodes. These advances underscore the potential of all-solid-state sodium-ion batteries (ASSSIBs) for achieving safe, stable, and sustainable energy storage solutions.

While substantial experimental research has focused on material development for ASSSIBs, theoretical studies have primarily targeted

* Corresponding author.
E-mail address: felix.gerbig@kit.edu (F. Gerbig).

https://doi.org/10.1016/j.egyr.2024.11.077
Received 8 August 2024; Received in revised form 17 November 2024; Accepted 26 November 2024
Available online 9 December 2024

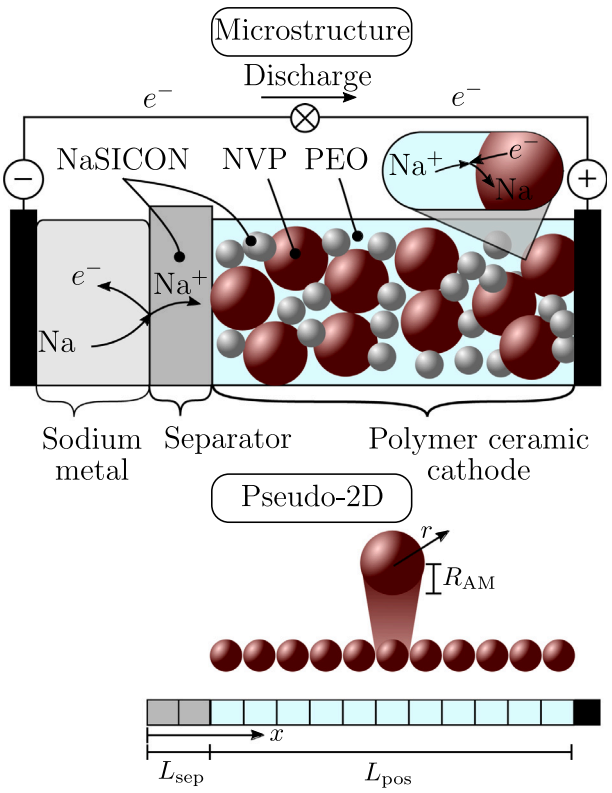

Fig. 1. Illustration of the working principle and idealized geometry of the P2D model for the battery system. The figure compares the detailed 3D representation of the battery system with its simplified 2D planar approximation used in the P2D model. This comparison highlights the model's ability to capture the multi-scale nature of physics-based battery simulations, illustrating how the P2D model streamlines complex 3D interactions into a more manageable 2D framework while maintaining essential details.

active materials and electrolytes at the molecular level (Åvall et al., 2018; Kim et al., 2022). Continuum models have been effectively employed to study particle properties in LIBs, enhancing understanding of otherwise inaccessible processes within the battery cell (Cernak et al., 2020; Goldin et al., 2012).

In our previous work, we employed a physics-based microstructure model to investigate the impact of cell composition on battery performance at the particle level in ASSSIBs with composite electrolytes (Gerbig et al., 2024). This approach provided detailed insights into factors such as ionic conductivity and reaction kinetics, contributing to a deeper understanding of transport and interphase phenomena. However, the high computational cost and complexity of microstructure-resolved simulations limit their use for multi-parameter optimization across broader design spaces.

In contrast, pseudo-two-dimensional (P2D) models, which rely on homogenized effective properties, offer a computationally efficient alternative for global optimization and large-scale simulations (Brosa Planella et al., 2022; Chayambuka et al., 2022). These models can replicate battery behavior accurately by integrating results from detailed microstructure simulations, enabling the exploration of cell designs and operating conditions at a fraction of the computational cost. For example, reduced-order models have been successfully developed for SIBs, combining the accuracy of P2D models with rapid computation times, making them ideal for multi-parameter optimization (Garapati et al., 2023).

This study builds on these advancements by combining the strengths of microstructure-based models and P2D simulations. Using results from microstructure simulations, we enhance the P2D model to capture the effects of composite hybrid electrolytes in ASSSIBs. This integrated approach enables the exploration of a broad parameter space, offering insights into the interplay of material properties, transport processes, and design factors. By addressing the challenges associated with solid-state systems, our work provides a foundation for optimizing the performance and sustainability of future sodium-ion batteries (Darjazi et al., 2024).

2. Model

The simulations in this study were performed using the Python Battery Mathematical Modeling (PyBaMM) software package, which utilizes the finite volume method (Sulzer et al., 2021). It is an open-source python software offering a framework for solving differential equations, a library of battery models and parameters, and specialized tools for conducting and visualizing battery-specific experiments, enabling users to explore different battery designs and assumptions under various operating conditions efficiently. The numerical solver employed in this study is derived from a base solver developed for lithium-ion batteries known as the DFN-model (Doyle et al., 1993), suitably adapted to model sodium ion batteries with hybrid electrolytes. The presented model uses concentrated solution theory to describe the potential and species distribution in a binary electrolyte (Thomas et al., 2002). In the P2D model, the electrode and the separator are simplified to a one-dimensional planar geometry, reducing the governing equations to their one-dimensional form. Additionally, the model accounts for Na diffusion within the active material particles along the radial dimension r assuming spherical electrode particles. The two dimensions are fully-coupled leading to the model's designation as the P2D model.

Fig. 1 illustrates the working principle of the battery system and the idealized geometry of the P2D model, which aims to capture the multi-scale nature of physics-based modeling

2.1. Governing equations

Polyanion sodium vanadium phosphate (NVP) is among the most extensively studied active materials for sodium-ion batteries (SIBs) due to its outstanding stability, promising capacity, and excellent cycle life (Chen et al., 2020). In this research, NVP is used as the active cathode material, with the overall reaction of the sodium-ion battery given by:

$$Na_3V_2^{III}(PO)_4 \rightleftharpoons NaV_2^{IV}(PO)_4 + 2Na^+ + 2e^- \tag{1}$$

The insertion electrode reaction is illustrated below, where Θ_s represents a location within the active material. This reaction occurs at a potential of about 3.4 V relative to Na^+/Na, involving the oxidation state change of $V^{3+/4+}$.

$$Na\Theta_s \rightleftharpoons Na^+ + \Theta_s + e^- \tag{2}$$

The mathematical model is based on five coupled equations that describe mass and charge conservation in both the solid insertion electrode and the electrolyte. In the active material, Ohm's law is used to represent the current density.

$$\boldsymbol{i}_s = -\sigma \nabla \Phi_s \tag{3}$$

where σ stands for the active material conductivity and Φ_s denotes the active material potential. NVP itself exhibits an electrical conductivity as low as 3×10^{-8} S cm^{-1} (Novikova et al., 2018). The model includes the conductivity-enhancing effect of carbon coating, resulting in a constant electrical conductivity. Assuming that electron movement is faster than other processes, the charge density remains stable $\frac{\partial \rho_V}{\partial t} = 0$, leading to the following continuity equation for the solid potential:

$$\nabla \cdot \left(-\sigma_{eff} \nabla \Phi_s\right) = -a_s j_{BV} \tag{4}$$

In the equation, the Butler–Volmer flux density (j_{BV}) is present as a source term on the right-hand side with the specific interfacial surface

area (a_s) as a prefactor, differing from microstructure models where j_{BV} is accounted for in the boundary conditions at the electrolyte–electrode interface. a_s describes the cathode–electrolyte interface area per unit volume. According to Fick's first law, the molar flux density of sodium is proportional to the concentration gradient. The continuity equation depending on the active material sodium diffusion coefficient (D_s) is then represented by Fick's second law. The sodium transport in a symmetrical spherical particle along the pseudo-dimension r is then given by:

$$\frac{\partial c_s}{\partial t} = \frac{1}{r^2}\nabla\left(r^2 D_s \frac{\partial c_s}{\partial r}\right) \tag{5}$$

The movement of sodium in the electrolyte is described using concentrated solution theory, which is considered to be more accurate than the simple dilute solution theory. The sodium flux in a binary electrolyte, which takes into account both diffusion and migration and depends on the electrolyte sodium ion diffusion coefficient (D_{el}), transference number of sodium ions in the electrolyte (t_+^0), electrolyte sodium ion concentration (c_{el}), Faraday constant (F), and electrolyte current density (i_{el}), is given by:

$$\boldsymbol{J}\, c_{el} = -D_{el}\left(1 - \frac{\mathrm{d}\ln c_{el,0}}{\mathrm{d}\ln c_{el}}\right)\nabla c_{el} + \frac{\boldsymbol{i}_{el} t_+^0}{F} \tag{6}$$

The convective term is excluded in this analysis because the solvent velocity in solid electrolytes is generally zero. A detailed derivation of the equation using the Maxwell–Stefan relationship can be found in Plett (2015). In this work, the thermodynamic factor $1 - \frac{\mathrm{d}\ln c_{el,0}}{\mathrm{d}\ln c_{el}}$ is assumed to be 1. From this, the mass conservation equation for the electrolyte is derived:

$$\frac{\partial\left(\varepsilon_{el} c_{el}\right)}{\partial t} = \frac{\partial}{\partial x}\left(D_{el,\,eff}\frac{\partial c_{el}}{\partial x}\right) + a_s\left(1 - t_+^0\right) j_{BV} \tag{7}$$

In the equation above, j_{BV} is present as a source term on the right-hand side with a sign opposite to that in Eq. (5). The volume-averaged charge transport in the electrolyte is given by the equation:

$$a_s F j_{BV} = -\frac{\partial}{\partial x}\left[\kappa_{eff}\frac{\partial \overline{\Phi_{el}}}{\partial x}\right] + \frac{\partial}{\partial x}\left[\kappa_{d,eff}\frac{\partial \ln \overline{c_{el}}}{\partial x}\right] \tag{8}$$

In this context, it is essential to account for the diminished electrolyte sodium ion diffusion coefficient and electrolyte ionic conductivity relative to the microscale model, attributable to tortuosity and porosity, reflected in their effective values (denoted by the subscript *eff*).

$$D_{el,eff} = D_{el}\frac{\varepsilon_s}{\tau} \tag{9a}$$

$$\kappa_{eff} = \kappa\frac{\varepsilon_s}{\tau} \tag{9b}$$

It is convenient to define the electrolyte diffusional conductivity as

$$\kappa_d = \frac{2RT\kappa}{F}\left(1 - t_+^0\right) \tag{10}$$

A fifth equation is necessary to solve the set of coupled partial differential equations (PDEs) and ordinary differential equations (ODEs). This equation calculates the rate of sodium production or consumption via the electrochemical surface reaction. It considers the essential charge transfer kinetics at the active material surface and within the electrolyte, conforming to the renowned Butler–Volmer equation (Bazant, 2023; Newman and Balsara, 2021).

$$\overline{j_{BV}} = \overline{i_0}\sinh\left(\frac{F}{2RT}\left(\overline{\Phi_s} - \overline{\Phi_{el}} - U_{eq}\left(\overline{c_s}\right)\right)\right) \tag{11}$$

The modeling approach captures the net charge transfer rate resulting from the heterogeneous reactions occurring at the electrolyte–cathode interface. The Butler–Volmer current density is dependent on the exchange current density (i_0), and the local overpotential. In the absence of detailed reaction mechanism information, the kinetic of the charge transfer reaction is typically assumed to be symmetric, setting the anodic and cathodic transfer coefficients, α_a and α_c, to 0.5. This assumption yields the following expression:

$$\overline{i_0} = Fk\sqrt{c_{s,max} - \overline{c_s}}\sqrt{\overline{c_s}}\sqrt{\overline{c_{el}}} \tag{12}$$

Here, i_0 describes the dynamic equilibrium of the charge transfer reaction, quantifying the electrons exchanged when the electrode is at rest. Typically, experimental measurements are required to determine the Butler–Volmer reaction constant (k), and the equilibrium potential (U_{eq}).

2.2. Boundary conditions

Selecting appropriate boundary conditions is crucial for solving the model. Charge is transferred via electronic current at the current-collector-electrode boundary ($x = L_{sep} + L_{pos}$) while no charge is transferred between the current-collector and the electrolyte. Because of charge conservation, the current at the current-collector must equal the total current. By similar reasoning, the electronic current at the electrode–separator boundary ($x = L_{sep}$) is zero because charge is only transported by ion movement in the electrolyte. The boundary conditions for the active material potential are accordingly:

$$\left.\frac{\partial\overline{\Phi_s}}{\partial x}\right|_{x=L_{sep}} = 0, \quad \text{and} \quad \left.\frac{\partial\overline{\Phi_s}}{\partial x}\right|_{x=L_{sep}+L_{pos}} = \frac{-i_{cell}}{\sigma_{eff}} \tag{13}$$

Here, the total cell current density (i_{cell}) is expressed as:

$$i_{cell} = \frac{I_{ap}}{A_{cc}} = CL_{pos}\varepsilon_s F\left(c_{s,max} - c_{s,min}\right) \tag{14}$$

The ionic current density at the current-collector-electrolyte boundary must be zero. We need to define a reference potential at the separator–electrolyte boundary, which is typically set to zero.

$$\left.\overline{\Phi_{el}}\right|_{x=0} = \Phi_{el,ref}, \quad \text{and} \quad \left.\frac{\partial\overline{\Phi_{el}}}{\partial x}\right|_{x=L_{sep}+L_{pos}} = 0 \tag{15}$$

The c_s gradient at the particle surface ($r = R_{AM}$) is proportional to the flux density resulting from the Butler–Volmer equation. The assumption of radially symmetrical particles demands the net flux at the center of the particles to be zero.

$$\left.\frac{\partial c_s}{\partial r}\right|_{r=0} = 0, \quad \text{and} \quad \left.\frac{\partial c_s}{\partial r}\right|_{r=R_p} = -\frac{\overline{j_{BV}}}{D_s} \tag{16}$$

The flux of the anion into the separator and the active material is zero. Instead, its diffusion is balanced by migration, which establishes the boundary conditions for electrolyte sodium ion concentration. Additionally, there must be no mass flux from the electrolyte into the current-collector

$$\left.\frac{\overline{c_{el}}}{\partial x}\right|_{x=0} = -\frac{\left(1 - t_+^0\right) i_{cell}}{D_{el,eff}F}, \quad \text{and} \quad \left.\frac{\overline{c_{el}}}{\partial x}\right|_{x=0} = 0 \tag{17}$$

2.3. Effective transport properties in the P2D model

In the P2D model, the electrolyte is treated as continuum. This means that within each control volume, the values of physical parameters, such as electrolyte potential (Φ_{el}) and D_{el} are assumed to be constant. This approach neglects any spatial variations within the control volume, simplifying the modeling of ion transport and potential distribution across the electrolyte. While this simplification is computationally efficient, it necessitates the development of theories to determine effective parameters that can represent the behavior of heterogeneous materials accurately. In a composite polymer–ceramic electrolyte, the heterogeneity arises from the distinct properties of the polymer and ceramic phases. To accurately model the electrolyte in a P2D framework, effective parameters must be derived to capture the combined behavior of these phases. Effective medium theories are often employed to calculate these effective parameters. These theories provide a way to estimate the macroscopic properties of a composite material based on the properties and volume fractions of its constituents. For instance, the effective ionic conductivity of a composite electrolyte can be determined by considering the conductivities of

the polymer and ceramic phases and their respective volume fractions. Similarly, the effective diffusivity can be derived using these theories, ensuring that the continuum model accurately reflects the heterogeneous nature of the electrolyte.

The Maxwell–Garnett (MG) model is a widely employed theoretical framework used to estimate the effective properties of a composite material consisting of two distinct phases, and it has been previously utilized to model composite polymeric electrolytes (Jamnik et al., 2006; Przyluski et al., 1995). The MG model is based on the assumption that the composite material consists of spherical inclusion particles embedded within a continuous host matrix. The phases are structurally invariant up to the phase boundary and do not exhibit any significant interfacial resistance. This means that the interface between the two phases does not impede the transfer of the property being measured, such as thermal or electrical conductivity:

$$q_{\text{eff}} = q_{\text{Pol}}\left[1 + \frac{d(q_{\text{Nas}} - q_{\text{pol}})\varphi_{\text{el, pol}}}{q_{\text{Nas}} + (d-1)q_{\text{pol}} - (q_{\text{Nas}} - q_{\text{pol}})\varphi_{\text{el, pol}}}\right] \tag{18}$$

The Maxwell–Garnett model (MG) calculates an effective value for a physical quantity (q) from the properties of the individual phases as well as the electrolyte polymer volume fraction ($\varphi_{\text{el, pol}}$) and the space dimension (d). The derivation assumes that the inclusion particles are spherical and uniformly distributed within the host matrix without overlap. In the case of the polymer–ceramic electrolyte, the ceramic particles represent the inclusion phase, while the polymer is the host phase.

A different model which gained popularity for granular materials or packed beds is the Zehner–Bauer–Schlünder model (ZBS) (Tsotsas and Martin, 1987; Rodrigues et al., 2023). This model is particularly useful for systems where the material consists of packed spherical particles, a common configuration in various engineering applications, including battery technology. The ZBS model is based on a unit cell approach where the properties of individual phases and the microstructural arrangement are taken into account (Blumberg and Schlünder, 1995). The model requires several parameters: properties of the individual phases, the electrolyte porosity (which equals $\varphi_{\text{el, pol}}$), the shape factor (C_{f}) and a γ that describes the relative contact area between particles. The shape factor has a value of 1.25 for spherical particles. This factor accounts for the geometry of the particles and how they pack together. The parameter γ represents the degree of flattening at the contact points between particles, influencing the charge and mass transfer across these contact areas. The equations are given in Eqs. (19a) to (19f):

$$\frac{\kappa}{\kappa_{\text{pol}}} = \left(1 - \sqrt{1-\varphi_{\text{el, pol}}}\right) + \sqrt{1-\varphi_{\text{el, pol}}}\left[\gamma k_{\text{P}} + (1-\gamma)k_{\text{c}}\right] \tag{19a}$$

$$\gamma = \frac{A_{\text{c}}}{A_{\text{f}} N_{\text{P}}} \tag{19b}$$

$$k_{\text{P}} = \frac{\kappa_{\text{fil}}}{\kappa_{\text{pol}}} \tag{19c}$$

$$k_{\text{c}} = \frac{2}{N}\left(\frac{B}{N^2}\frac{k_{\text{P}}-1}{k_{\text{P}}}\ln\frac{k_{\text{P}}}{B} - \frac{B+1}{2} - \frac{B-1}{N}\right) \tag{19d}$$

$$N = 1 - \frac{B}{k_{\text{P}}} \tag{19e}$$

$$B = C_{\text{f}}\left(\frac{1-\varphi_{\text{el, pol}}}{\varphi_{\text{el, pol}}}\right)^{10/9} \tag{19f}$$

The flattening coefficient (γ) can either be empirically evaluated or approximated from the total contact area of the domain (A_{c}), the contact area between two particles (A_{f}) and the number of particles (N_{P}). The equations include the calculation of the dimensionless parameters ratio of ionic conductivities of dispersed and continuous phase in the ZBS model (k_{P}) and the reduced core ionic conductivity in the ZBS model (k_{c}). These equations encapsulate the detailed balance between the contributions from the particles themselves and the contact points between them, adjusted by the shape factor and porosity. Interestingly, both the ZBS model and the Maxwell–Garnett model are independent of the particle radii, focusing instead on the volumetric properties and the spatial arrangement of the particles. This independence from particle size simplifies the application of these models to various granular and composite materials.

2.4. Model parameterization

The physics-based model in this study employs a number of physical parameters, ideally either directly measured or derived from experimental data. These parameters, listed in Table 1, are primarily sourced from prior research (Gerbig et al., 2024). Briefly, the hybrid electrolyte comprises NaSICON particles incorporated within a PEO:nNaTFSI polymer matrix. While most parameters remain constant, the equilibrium potential plays a crucial role in shaping the polarization curves and is specific to the active material utilized. However, a robust theoretical framework for the sodium ion intercalation process remains elusive. This is due to deviations of the equilibrium potential for Na^+ intercalation electrodes from the predictions of the Nernst equation, attributed to solid-state redox reactions. Consequently, an anomalous voltage behavior is observed, a subject extensively explored and debated in existing literature (Chen et al., 2020; Si et al., 2014). The U_{eq} is contingent upon the mole fraction (χ) of intercalated species and is expressed as shown in the following equation:

$$FU_{\text{eq}} = FU_{\text{eq}}{}^{0} + RT\ln\left(\frac{1-\chi}{\chi}\right) + RT\left[-A + 2A\chi - B + 3B\chi - \frac{3}{2}B\chi^2\right] \tag{20}$$

Furthermore, the concentration dependency of the electrolyte ionic conductivity (κ) in a pure polymer electrolyte is elucidated through a semi-empirical equation, inspired by the work of Mongcopa et al. (2018), and calibrated against experimental data.

$$\kappa\left(c_{\text{el}}\right) = \kappa K_{\text{NaTFSI}}(T)c_{\text{el}}\left[\exp\left(-\frac{c_{\text{el}}}{c_{\text{el},\kappa_{\max}}(T)}\right)\right] \tag{21}$$

2.5. Computational solution

Throughout the discharge process, Eqs. (5) to (7) depict the motion of Na originating from the anode, passing through the electrolyte as Na^+, and eventually intercalating in the cathode's active material. In parallel, charge and ionic conservation in the cathode and electrolyte, respectively, are managed via electric and ionic potentials. In the pseudo-2D model, the sodium mass is simplified to a single scalar, representing Na^+ in the electrolyte and Na within the electrode. The system of equations is discretized into a system of DAEs by use of the PyBaMM software package (Sulzer et al., 2021) and then solved with the CasADi solver (Andersson et al., 2019)

3. Results and discussion

This section presents the impacts of polymer–ceramic cathode electrode characteristics on the battery performance, as predicted by the P2D model. In a first step, we compare results of the P2D model with microstructure simulations from previous work (Gerbig et al., 2024). Through computational simulations, we explore how various properties of the cathode electrode, such as composition, and thickness, may influence the overall performance metrics of the battery system. By analyzing these predictions, we seek insight into the underlying mechanisms that govern battery behavior, with the aim of informing future design strategies for enhanced battery performance.

Table 1
Modeling parameters for a hybrid sodium-ion battery cathode half-cell with a polymer–ceramic hybrid electrolyte at room temperature.

Parameter	Value	Reference
U_{eq} model parameter A	1.5837	Gerbig et al. (2024)
U_{eq} model parameter B	0.2306	Gerbig et al. (2024)
Symmetry factors (α_a, α_c)	0.5	[a]
Separator thickness (L_{sep})	50 µm	[a]
Sodium max concentration ($c_{s,max}$)	14.2 mol L^{-1}	[b]
Sodium min concentration ($c_{s,min}$)	0 mol L^{-1}	[b]
Butler–Volmer reaction rate constant k	3 ×10^{-12} m$^{2.5}$ mol$^{0.5}$ s^{-1}	Gao et al. (2017)
NVP/C conductivity (σ)	7.14 S cm^{-1}	Liu et al. (2019)
NaSICON conductivity (κ_{NAS})	1.5×10^{-3} S cm^{-1}	Kaus et al. (2017)
Polymer conductivity (κ_{pol})	6×10^{-5} S cm^{-1}	Serra Moreno et al. (2014)
NaSICON diffusion coefficient ($D_{el,NAS}$)	4×10^{-12} m^2 s^{-1}	Moradipour et al. (2023)
Polymer diffusion coefficient ($D_{el,pol}$)	4.7×10^{-14} m^2 s^{-1}	Wróbel et al. (2021)
Sodium-ion transference number (t_+^0)	0.39	Serra Moreno et al. (2014)
Bruggeman's exponent (b_{Brug})	−0.5	Bruggeman (1935)

[a] Geometric parameters used for simulation.
[b] Calculated based on gravimetric capacity reported in Zheng et al. (2017).

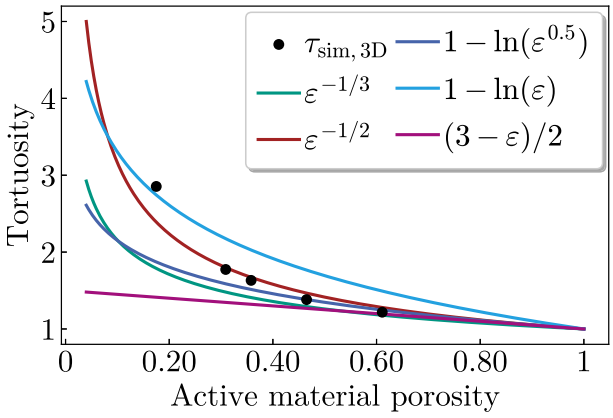

Fig. 2. Comparison of tortuosity versus porosity relationships for porous materials. The graph displays analytical solutions based on the Bruggeman equation and effective medium theory, juxtaposed with discrete values obtained from simulations of virtual electrodes using the microstructure model.

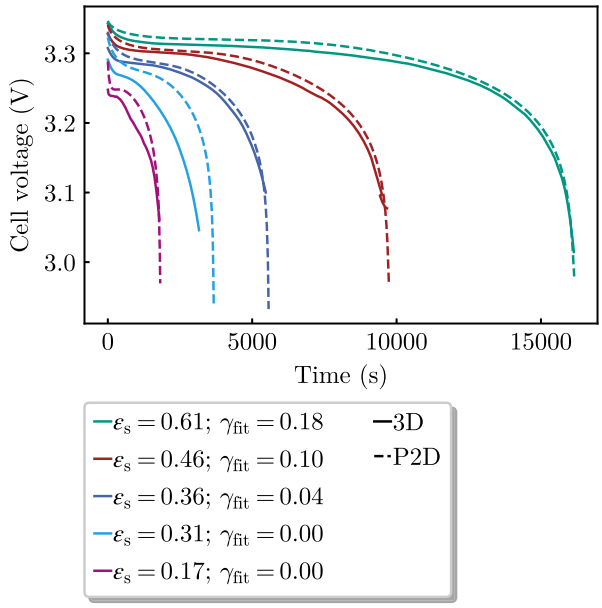

Fig. 3. Determination of the flattening coefficient (γ) for parameterizing the ZBS model. The figure illustrates the comparison of voltage curves obtained from particle-resolved microstructure simulations with those from the P2D model across various values of γ. The plot shows the voltage curves for different active material porosities, demonstrating the impact of γ on model accuracy and the effectiveness of the P2D model in replicating microstructure simulation results.

3.1. Evaluation of P2D model parameters

3.1.1. Tortuosity estimation

The Bruggeman equations, which are widely utilized, link the tortuosity factors of porous materials to their porosity. The electrode tortuosity (τ) is represented by the equation:

$$\tau = \varepsilon_s^{\,b_{Brug}} \tag{22}$$

A b_{Brug} value of −0.5 is anticipated for spherical particles, commonly applied in insertion batteries. To validate this hypothesis, we compared the tortuosity of virtual electrodes obtained from our microstructure model with established equations for tortuosity in porous media. The tortuosity simulated from the 3D model ($\tau_{sim,3D}$) is derived using Eq. (9b) from our methodology. Fig. 2 displays several correlations between porosity and tortuosity based on effective medium theory (Shen and Chen, 2007), alongside comparisons with tortuosity data from our microstructure model. It becomes evident from the data that the expression $\varepsilon^{-1/2}$, which corresponds to the Bruggeman correlation with the common exponent of −0.5, provides the best fit. Consequently, this relationship is implemented in the P2D model discussed in this paper.

3.1.2. Flattening coefficient estimation

As indicated in Eqs. (19a) through (19f), determining the flattening coefficient (γ) is essential for fully parameterizing the ZBS model. To achieve this, we compare results from a particle-resolved model with those from the proposed P2D model, aiming to find the optimal γ value. The polarization curves of the particle-resolved microstructure model are taken from a previous study (Gerbig et al., 2024). We vary γ from 0 to 1 in 1% increments and use a least-squares algorithm to assess the quality of the fit for each value of γ. Fig. 3 shows the voltage curves obtained from the microstructure simulations and the P2D simulations with the optimal flattening coefficient for different active material porosity.

For active material porosity (ε_s) in the range of 0.39 to 0.64, the results of the 3D simulation are successfully replicated by appropriately selecting flattening coefficients. However, for ε_s values from 0.69 to 0.83, the P2D simulations fail to fit the 3D simulations, as the simulated cell voltage remains higher even with $\gamma = 0$. The values of γ decrease from 0.16 to 0.03 as the active material porosity decreases from 0.64 to 0.39. This observation contradicts expectations because one interpretation of the flattening coefficient is the ratio between contact area and total particle surface area. To decrease the void volume of a virtual (or real) cathode — and thus the porosity — stronger compression is

Table 2
Fit parameters and quality assessments for the flattening coefficient.

ε_s	$\kappa_{eff,3D}$ (mS m^{-1})	γ	$\kappa_{eff,ZBS}$ (mS m^{-1})	dev (%)	$\kappa_{eff,MG}$ (mS m^{-1})	dev (%)
0.61	15.9	0.18	13.8	15.2	9.75	63.1
0.46	8.7	0.10	9.2	−4.5	6.45	34.9
0.36	5.4	0.04	5.7	−5.3	4.36	23.9
0.31	3.7	0	4.5	−27.8	3.5	5.7
0.17	1.1	0	1.5	−36.7	1.21	−9.1

needed. Particularly for porosities lower than the close-packing of equal spheres, significant deviations from a spherical shape and overlapping are required. This should result in an increasing flattening coefficient, yet the results indicate the opposite. A possible explanation is that the ZBS model was designed for heat conduction in fixed-beds considering two phases: a heterogeneous and a homogeneous conducting phase. In our battery model, the active material represents a third, from the electrolyte point-of-view, inert phase. Although the model considers lengthened transport paths and reduction of conductive volume by electrode tortuosity and active material porosity, other effects might occur. With lower ε_s a more uneven distribution of the electrolyte filler particles is likely. This can cause the interruption of conductive paths due to particles not being in contact with each other. At high compression rates, the gaps between two active material particles can become very small, making it difficult to fill with active material particles. In extreme cases, this can lead to unconnected, highly conductive islands of filler particle agglomerates connected by low-conductive polymer. Such a scenario cannot be described with the ZBS model and its assumptions.

However, within the ε_s interval of 0.31 to 0.61, the γ parameter, derived from fitting the cell voltage curves, demonstrates a linear relationship with active material porosity, showing $R^2 = 0.9988$:

$$\gamma = -0.5579\varepsilon_s - 0.1593 \tag{23}$$

Table 2 presents the effective electrolyte ionic conductivity for various ε_s attained from the 3D simulations, and compares these with values computed from both the ZBS model and the MG model. In the ZBS model, γ is selected to achieve the optimal fit for the cell voltage curves. The discrepancy in κ between the P2D simulations and the 3D simulations in the ε_s interval of 0.36 to 0.61 is less than 15.2% for the ZBS model, but exceeds 23.9% for the MG model. For lower active material porosity values, the ZBS model forecasts electrolyte ionic conductivity to deviate by more than 27.8% from the $\kappa_{eff,3D}$, while the MG model predicts a deviation of less than 9.1%. These observations align with the results from the cell voltage curve fits (Fig. 3) and recommend the use of the ZBS model with γ as determined by Eq. (23) for medium to high active material porosities. For batteries with low values of ε_s, the effective electrolyte ionic conductivity is more accurately represented by the MG model. This implies that such an electrode is in a regime where the electrolyte active filler particles are not closely packed. For subsequent simulations, the model for calculating κ is selected based on ε_s. A sigmoid function is employed to ensure a smooth transition between the MG and ZBS models at $\varepsilon_s = 0.31$.

3.2. Effect of electrolyte active filler content

An important property of a battery with a composite electrolyte is the ratio of host and inclusion material. The $\varphi_{el,\,fil}$ specifically represents the proportion of polymer within the electrolyte phase, which comprises polymer and fillers. Fig. 4 presents the discharge process of the studied battery system, wherein the NaSICON-type active filler content in the electrolyte is varied. The NVP content is maintained at 50%, with a cathode length of 100 µm providing a theoretical specific capacity of 204 mA L^{-1}. In subsequent investigations, $\varphi_{el,\,fil}$ was varied from 0% to 100%. The simulations are conducted at different C-rates from 0.05 C to 10 C, and the Depth of Discharge (DoD) is reported.

For discharging with a very low C-rate of 0.05 C, electrodes with $\varphi_{el,\,fil}$ greater than 0.3 achieve 100% utilization. At C-rates of 0.5 C and

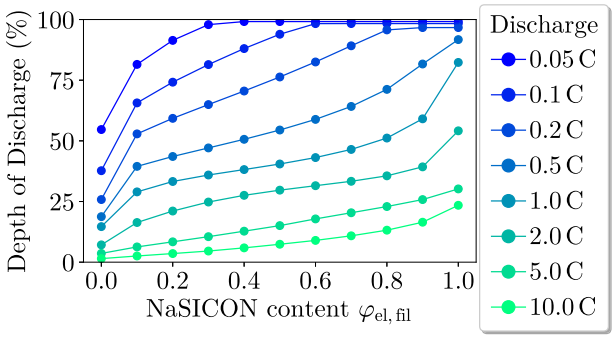

Fig. 4. Effect of electrolyte electrolyte active filler volume fraction ($\varphi_{el,\,fil}$) on the discharging performance of the battery system. The figure shows the impact of varying the NaSICON-type active filler content within the composite electrolyte, while maintaining a 50% NVP content and a cathode length of 100 µm. The theoretical specific capacity is 204 mA L^{-1}. Simulations were performed at different C-rates (ranging from 0.05 C to 10 C), and the resulting Depth of Discharge (DoD) is presented.

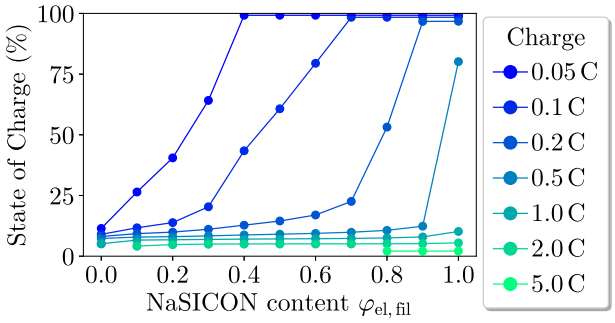

Fig. 5. Effect of electrolyte electrolyte active filler volume fraction ($\varphi_{el,\,fil}$) on the charging performance of the battery system. The figure shows the impact of varying the NaSICON-type active filler content within the composite electrolyte, while maintaining a 50% NVP content and a cathode length of 100 µm. The theoretical specific capacity is 204 mA L^{-1}. Simulations were performed at different C-rates (ranging from 0.05 C to 5 C), and the resulting State of Charge (SoC) is presented.

higher, complete utilization is not achieved even with a pure NASICON electrolyte. Generally, battery capacity utilization increases with $\varphi_{el,\,fil}$, with the increase being more pronounced at lower C-rates. For C-rates of 1.0 C and above, satisfactory utilization is not achieved by adding NASICON fillers, with the DoD remaining below 50% in all cases.

The effect of filler content on the charge process is shown in Fig. 5. The results differ significantly from the discharge process, with utilization drastically decreasing as C-rates increase. For instance, an electrode charged at 0.5 C utilizes only 10% of its capacity for most $\varphi_{el,\,fil}$ values, compared to approximately 50% utilization during discharging. This distinct behavior can be attributed to transport limitations in the electrolyte. At the beginning of the charging or discharge process, most charge transfer reactions occur near the separator. During charging, the reaction consumes Na^+ in the electrolyte, leading to the depletion of charge-carrying species and an abrupt termination of the charge process if charge and mass transport within the electrolyte are insufficient.

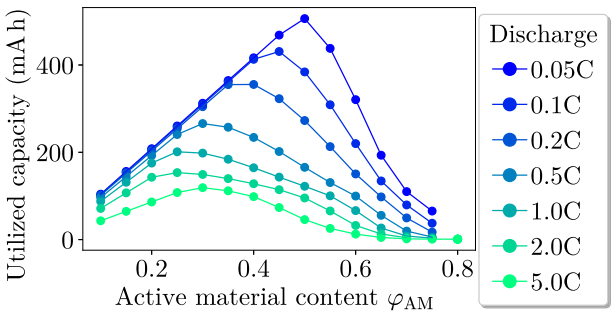

Fig. 6. Utilized capacity as a function of active material content (φ_{AM}) during the discharge process at different C-rates from 0.05 C to 5 C and a constant electrolyte active filler volume fraction of 50%.

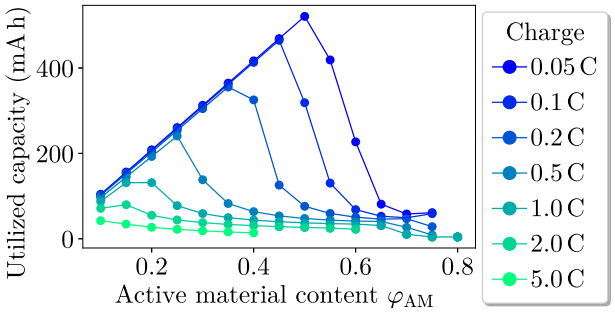

Fig. 7. Utilized capacity as a function of active material content (φ_{AM}) during the charge process at different C-rates from 0.05 C to 5 C and a constant electrolyte active filler volume fraction of 50%.

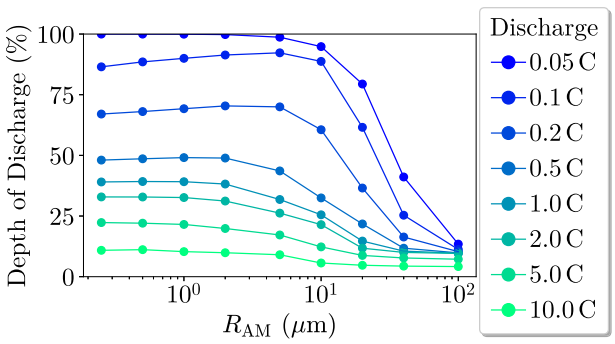

Fig. 8. Depth of discharge as a function of active material particle radius (R_{AM}) during the discharge process. The figure demonstrates the impact of particle size on battery performance for an electrode with 50% active material content and a cathode length of 100 µm.

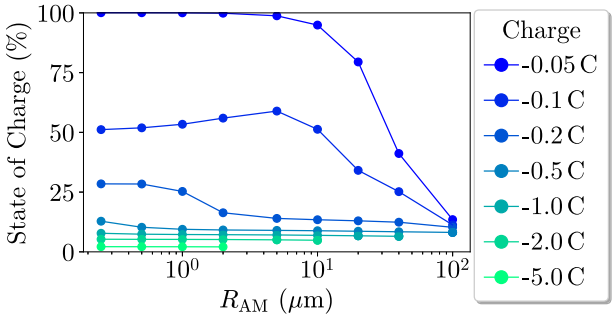

Fig. 9. State of charge as a function of active material particle radius (R_{AM}) during the charge process. The figure demonstrates the impact of particle size on battery performance for an electrode with 50% active material content and a cathode length of 100 µm.

3.3. Effect of electrode porosity

The φ_{AM} is a critical parameter in the design and optimization of battery system. Elevated levels of φ_{AM} are advantageous as they enhance the theoretical capacity of the battery, leading to improved energy storage capabilities. However, beyond a certain threshold, the utilization efficiency of the resources used to build the battery system diminishes due to transport limitations arising within both the electrode and the electrolyte. These limitations hinder ion and electron movement, thereby affecting the overall performance and longevity of the battery. The occurrence of these limitations is highly specific to the materials used, and thus, their impact on the discussed battery system will be explored in the following section.

Fig. 6 illustrates the utilized capacity as a function of φ_{AM} for cathode electrodes at various C-rates during the discharge process. The battery features a cross-sectional electrode area of 0.028 m^2 and $\varphi_{el,\,fil}$ of 50%. For all C-rates, the simulated electrodes exhibit low utilized capacity at low φ_{AM} values, which increase with higher φ_{AM} before declining again. For electrodes with low φ_{AM}, the utilized capacity is limited by the theoretical capacity, whereas those with high φ_{AM} experience transport limitations in the electrolyte. This is attributed not only to the reduced electrolyte volume but also to increased tortuosity and the greater total current that needs to be transported. The optimal φ_{AM} varies with the C-rate: an active material content of 0.5 is optimal for a 0.05 C discharge, while 30% φ_{AM} is optimal for a 5 C discharge.

Fig. 7 depicts the utilized capacity for various φ_{AM} and C-rates during the charge process. When φ_{AM} exceeds the optimal level, the utilized capacity decreases more sharply compared to discharging. Additionally, for C-rates above 0.2 C, the utilized capacity is relatively low, consistent with the findings from the study on $\varphi_{el,\,fil}$ variation in Section 3.2.

3.4. Effect of active material particle size

The particle size of the active material in batteries is a fundamental morphological parameter that is relatively easy to control and measure, compared to properties such as surface roughness, shape, and internal porosity. Consequently, it attracts significant attention in battery research and development. While in practical applications, active material particles exhibit a size distribution, our study employs monodisperse particles to isolate and better understand the specific influence of particle size on battery performance.

Fig. 8 illustrates the depth of discharge at the conclusion of the discharge process for an electrode with an φ_{AM} of 50% and a cathode length of 100 µm across different active material particle radii from 0.25 µm to 100 µm. The depth of discharge remains approximately constant for R_{AM} values smaller than 2 µm and declines sharply for R_{AM} larger than 10 µm. This pattern holds true for all C-rates, with the depth of discharge leveling off at higher values for lower C-rates. This behavior is due to transport limitations in the electrolyte that are unaffected by R_{AM}.

The achieved SoCs for the charge process with varying R_{AM} is shown in Fig. 9. As seen in the previous sections, the capacity utilization of the charge process is reduced for C-rates above 0.2 C. Like in the discharge process, the achievable state of charge remains nearly unchanged for R_{AM} values below 2 µm and drops significantly for R_{AM} values greater than 10 µm.

The research indicates that an R_{AM} of 4 µm is optimal, as decreasing the particle size further does not substantially improve performance. Additionally, smaller particles are generally more challenging to manufacture and handle during the production process. They may also reduce electrical conductivity within the electrode due to the increased number of particle–particle contacts.

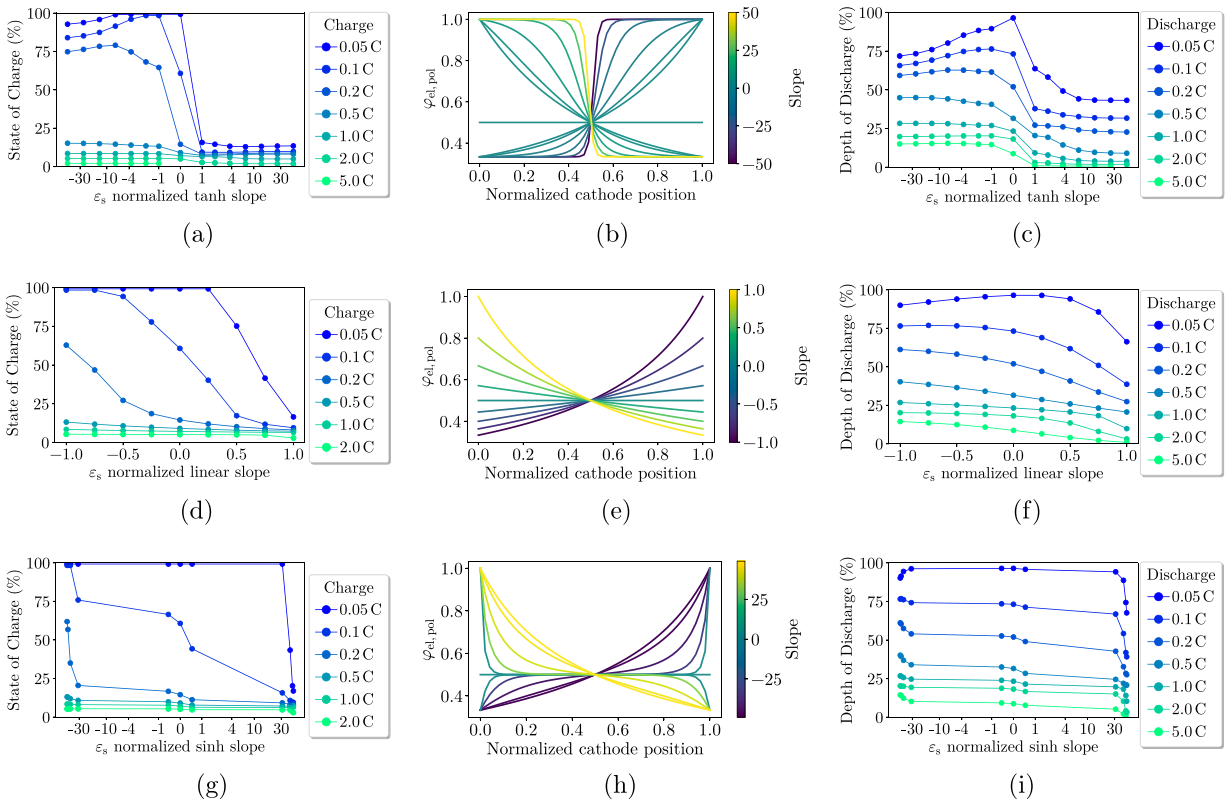

Fig. 10. Performance comparison of different active material (φ_{AM}) and active filler φ_{fil} distributions within the positive electrode during charging and discharge processes. The figure is organized into three columns and three rows:
• **Left Column** (Figs. 10(a), 10(d) 10(g)): State of charge (SOC) at the end of the discharge process for electrodes with tanh, linear, and sinh distributions of the active material porosity. The SOC is plotted against the slope parameter of the respective distribution function.
• **Middle Column** (Figs. 10(b), 10(e) 10(h)): Resulting distribution of polymer volume fraction (φ_{pol}) within the half-cell. The tanh, linear, and sinh distributions are shown, illustrating the variations in φ_{pol} with different slope parameters.
• **Right Column** (Figs. 10(c), 10(f), 10(i)): Depth of discharge (DoD) at the end of the discharge process for electrodes with the same distributions of the active material porosity. (For interpretation of the references to color in this figure legend, the reader is referred to the web version of this article.)

3.5. Effect of spatial active filler content variation

The previous chapters maintained a constant distribution of active material and active filler within the positive electrode. However, observations suggest that battery processes, such as charge transfer reactions, occur unevenly within the electrode, often concentrated in specific areas. This raises the question of whether non-uniform material distribution could enhance performance.

In the present study, the ratios of active material particles and active filler particles are varied while maintaining average values of $\overline{\varphi_{AM}} = 0.5$ and $\overline{\varphi_{fil}} = 0.25$. The φ_{pol} remains constant throughout the half-cell with ($\overline{\varphi_{pol}} = 0.25$). Consequently, only the ratio of active material to active filler particles varies across the cathode compartment. This investigation explores distributions using hyperbolic tangent (tanh), linear, and hyperbolic sine (sinh) functions with different slopes. The tanh distribution function is defined in Eq. (24) where the parameter a determines the slope:

$$\varphi_{AM} = \begin{cases} \overline{\varphi_{AM}} & \text{for } a = 0 \\ \frac{\min(\overline{\varphi_{fil}}, \overline{\varphi_{AM}})}{\tanh\frac{|a^*|}{2}} \tanh\left(a\frac{\frac{L_p}{2} - x_p}{L_p}\right) + \overline{\varphi_{AM}} & \text{for } a \neq 0 \end{cases} \tag{24}$$

This function approximates a step function for large a values and a linear function for values close to zero.

The linear distribution function, defined in Eq. (25), ensures physical validity of φ_{AM} with a ranging from −1 to 1:

$$\varphi_{AM} = -2a \min\left(\overline{\varphi_{fil}}, \overline{\varphi_{AM}}\right) \frac{x_p}{L_p} + \overline{\varphi_{AM}} + a\overline{\varphi_{fil}} \qquad -1 \le a \le 1 \tag{25}$$

Eq. (26) describes the sinh distribution of φ_{AM}. When a has large values, the function approximates a nearly constant distribution of φ_{AM} with sharp gradients at both extremities of the half-cell. For small a values close to zero, the function resembles a linear distribution.

$$\varphi_{AM} = \frac{\min\left(\overline{\varphi_{fil}}, \overline{\varphi_{AM}}\right)}{\sinh\frac{|a^*|}{2}} \sinh\left(a^* \frac{\frac{L_p}{2} - x_p}{L_p}\right) + \overline{\varphi_{AM}} \qquad \text{with}$$

$$a^* = \operatorname{sgn}(a)\,(a_{max} - |\,a\,|) \tag{26}$$

Besides φ_{AM} the solver needs $\varphi_{el,\,pol}$ to calculate the distribution of the effective transport properties in the electrolyte:

$$\varphi_{el,\,pol} = \frac{\overline{\varphi_{pol}}}{1 - \varphi_{AM}} \tag{27}$$

The distribution of φ_{pol} is illustrated in the middle column of Fig. 10 (Figs. 10(b), 10(e), and 10(h)). The left column (Figs. 10(a), 10(d), and 10(g)) shows the state of charge achieved at the end of a discharge process simulated with electrodes having tanh, linear, and sinh distributions of ε_s. The state of charge is plotted against the slope of the respective distribution, while the length of the positive half cell remains constant at 100 µm. Different colored lines represent charge processes with different C-rates.

For all distributions, a negative ε_s slope leads to a higher achievable state of charge than a positive slope. A negative ε_s slope means that ε_s is high near the separator (normalized cathode position = 0), allowing more space for active filler particles, which results in lower $\varphi_{el,\,pol}$. Conversely, ε_s decreases near the cathode current collector (normalized cathode position = 1), leading to high $\varphi_{el,\,pol}$ due to the lack of space for active filler particles.

Table 3
Gravimetric properties of the battery.

Parameter	Value	Reference
ϱ_{PEO}	1250 kg m^{-3}	Teran and Balsara (2014)
ϱ_{fil}	3170 kg m^{-3}	Fuentes et al. (1999)
$\varrho_{NVP,C}$	3200 kg m^{-3}	Zeng et al. (2017)
ϱ_{CC}	0.012 kg m^{-2}	Chun et al. (2023)
N/P	1	Yim et al. (2023)

With 0.05 C and 0.1 C charging, all distributions reach 100% utilization. The sinh distribution performs best with a large negative slope, closely approximating a linear distribution, indicating that a sinh distribution is not advantageous over a linear one for charging. The battery with a tanh distribution achieves a state of charge exceeding 75% for moderately negative slopes and a 0.2 C charge, showing a 15% improvement over the linear ε_s distribution. For C-rates higher than 0.2 C, none of the distributions achieves a satisfactory state of charge.

The depth of discharge at the end of discharging for a battery with tanh, linear, and sinh ε_s distributions is shown in the right column (Figs. 10(c), 10(f), and 10(i)). For a 0.05 C discharge, $a = 0$ results in the highest depth of discharge, corresponding to a constant value of ε_s and $\varphi_{el,\ pol}$.

Similar to the charge process, a negative ε_s slope increases the achievable depth of discharge for C-rates above 0.05 C for all three distributions. However, the increase in depth of discharge is less than during charging, ranging from 0% to 10%. Both the sinh and tanh distributions do not lead to better utilization than a simpler linear distribution. According to simulation results, a normalized linear slope of −1 is optimal. This describes a positive half-cell with high porosity at the separator, linearly decreasing towards the current collector.

3.6. Global optimization of the cell-design

The earlier sections emphasized altering one influencing parameter at a time. While this method aids in forming a deeper comprehension of the battery system and forecasting parameters to improve battery performance, it is unlikely to achieve a globally optimal battery design. This is because a battery is a highly interconnected and non-linear system with many input parameters affecting each other. One benefit of the P2D model is its brief computational time and cost, making it suitable as a cost function in a global optimizer. A differential evolution algorithm (Storn and Price, 1997) is appropriate for this kind of optimization. Although it demands more function evaluations than traditional gradient-based methods, it can search large candidate spaces and avoid local minima due to its stochastic nature. We utilized the Python package scipy, version 1.12.0. The objective function is the P2D model of the all-solid-state sodium-ion battery with a hybrid electrolyte, which provides the utilized gravimetric capacity. Input parameters include φ_{AM}, linear slope of the spatial active material distribution a, and L_{pos}. The R_{AM} is excluded from the optimization because the study in Section 3.4 indicated a monotonic relationship between R_{AM} and capacity utilization, causing the optimizer to select the lower limit. Practically, an exceedingly small R_{AM} value is undesirable because it complicates manufacturing, processing, and increases the grain boundary surface. This aspect could be incorporated into the optimization by adding another objective. We sidestep a multi-objective optimization by constraining R_{AM} to a user-defined value using the ε-constraint method (Haimes, 1973). This method is validated by the finding that $R_{AM} < 4\,\mu m$ does not enhance performance. Although it is feasible to achieve thin NaSICON separators as technology matures, a value of 5×10^{-3} µm is adopted for L_{sep} owing to its fragility.

Table 3 lists the densities of the battery materials used, including the compartment. The thickness of the separator and the current collector is independent of the length of the positive half cell. It is crucial to include these components in the optimization to dissuade the algorithm from selecting overly thin electrodes. Determining the overall gravimetric capacity is straightforward by using the densities, volume fractions, and the utilized capacity.

Table 4
This table presents the outcomes of global optimization for all-solid-state sodium-ion batteries across various C-rates, specifically from 0.05 C to 0.5 C. It provides a summary of the optimal design parameters, such as the volume fraction of active material (φ_{AM}), electrode thickness (L_{pos}), and the linear slope of the spatial active material distribution (a), applicable to both charging and discharging phases. Additionally, the table emphasizes the achieved capacity utilization for each C-rate, revealing the differences and compromises in battery performance. For each C-rate, the optimized design parameters are juxtaposed with those obtained from individual optimizations of charging and discharging phases, offering insights into performance constraints and the benefits of the global optimization method.

C	φ_{AM}	a	L_{pos} (µm)	Used capacity (A h kg^{-1})
Discharging				
0.05	0.477	−0.00	97.2	37.8
0.1	0.448	−0.01	79.9	32.4
0.2	0.429	−0.22	66.2	27.3
0.5	0.370	−0.28	56.1	20.6
Charging				
0.05	0.566	−0.62	117.3	47.8
0.1	0.543	−0.71	101.5	43.2
0.2	0.547	−0.72	79.6	38.5
0.5	0.525	−0.77	61.6	31.1
Charging and Discharging				
0.05	0.478	−0.03	97.34	37.83
0.1	0.445	−0.20	85.6	32.3
0.2	0.401	−0.18	75.6	27.2
0.5	0.372	−0.30	56.5	20.5

The outcomes of the optimization using the physical properties stated earlier n Table 1 for C-rates spanning from 0.05 C to 0.5 C are presented in Table 4. Despite earlier chapters' parameter studies forecasting a greater overall capacity utilization for the discharge process, the optimization indicates that, for an optimal selection of cell design parameters, the charge process harnesses more capacity than discharging. The charging capacity is 10.5 A h kg^{-1} or 51% higher at 0.5 C and 10 A h kg^{-1} or 26.5% higher at 0.05 C when compared to discharging. This phenomenon occurs because the electrodes are thicker during charging, specifically 5.4 µm thicker for 0.5 C and 19.9 µm thicker for 0.05 C, than during discharging. Additionally, the φ_{AM} for charging is higher, 0.155 for 0.5 C and 0.089 for 0.05 C, as opposed to discharging. Generally, L_{pos} and φ_{AM} reduce as the C-rate increases, ranging from 117.3 µm to 61.6 µm and 0.566 to 0.525 for charging and from 97.2 µm to 56.1 µm and 0.477 to 0.370 for discharging. The magnitude of the slope (a) of the active material particle and the active filler particle distribution increases with increasing C-rate of −0.62 to −0.77 for charging and from 0 to −0.28 for discharging. The results of combination of the charging and discharging optimization are shown in the last section of Table 4. For each parameter combination, both charging and discharge processes were simulated, and the used capacity was evaluated, with the lower value being reported to represent the limiting factor. The simulations predict a nearly equal used capacity for the combined charging and discharging cycled compared to the discharging cycle alone. While these findings seem initially appear intuitive, given that the discharging cycle demonstrated lower utilization in the optimization study, a closer examination reveals a more nuanced picture.

First, the parameter studies in earlier sections indicated that the charge process is highly sensitive to the input parameters, leading to an abrupt early termination if the parameters are poorly chosen. Second, the optimization for combined charging and discharging results in a different set of input parameters for some C-rates compared to the optimization for discharging alone. Specifically, for C-rates of 0.1 and 0.2, a battery optimized for charging and discharging is thicker with lower values of φ_{AM}.

The global cell design optimization leads to several key conclusions: Even for low to moderate C-Rates the optimal cell design strongly depends on the C-rate. Higher C-rates demand lower φ_{AM}, L_{pos} and a more uneven distribution of particles with a increased porosity near the separator. Secondly, optimizing the design separately for charging and discharging results in distinct cell configurations. Notably, a battery optimized for both charging and discharging performs equally well as a discharging-optimized design, highlighting the discharge process as the bottleneck for achieving high capacity utilization.

4. Summary and conclusion

Efficient cell design is critical for the performance and resource efficiency of all-solid-state sodium-ion batteries (ASSSIBs). This study developed and parameterized a pseudo-two-dimensional (P2D) model, integrating insights from microstructure models to understand the interplay between cell composition, transport phenomena, and battery performance in hybrid polymer–ceramic electrolytes. The findings reveal that at low C-rates (0.05 C), cells with an electrolyte active filler volume fraction exceeding 0.3 achieve full utilization. However, at higher C-rates (0.5 C and above), even pure NaSICON electrolytes do not enable full utilization, particularly during charging. This limitation arises from the depletion of charge carriers near the separator, leading to abrupt termination of the process.

The active material content is shown to have a strong influence on capacity utilization, with an optimal value dependent on the C-rate. For discharging, the optimal active material content is approximately 0.5 at 0.05 C, decreasing to 0.3 at 5 C. Exceeding this optimal value results in reduced performance due to transport limitations, with a more pronounced effect during charging. Simulations also highlight the importance of active material particle radius, identifying 4 µm as an optimal size. Larger particles exacerbate transport limitations, reducing performance, while smaller particles, although theoretically advantageous, pose practical challenges in manufacturing and handling and may decrease electrical conductivity due to increased particle–particle contacts.

Spatial porosity distributions within the electrode were also investigated by varying the distribution of active material particles and filler particles while maintaining constant average values. Results indicate that electrodes with higher porosity near the separator, modeled using a linear distribution, perform better, particularly at moderate C-rates. At higher C-rates, none of the tested distributions achieved satisfactory utilization, but the linear distribution with a normalized slope of −1 proved to be optimal for low to moderate C-rates.

The optimization study underscores the intricate, non-linear interplay of parameters in achieving globally optimal ASSSIB designs. Charging and discharging exhibit distinct optimal cell configurations, but cell designs optimized for both processes perform comparably to those optimized for discharging, identifying it as the bottleneck for capacity utilization. These findings suggest that optimized designs must balance active material fraction, porosity distribution, and particle size, while also accounting for the distinct requirements of charging and discharging processes.

Overall, this study provides critical insights into the design of ASSSIBs with hybrid polymer–ceramic electrolytes. The P2D model, with its computational efficiency, is shown to be an effective tool for optimizing cell designs and guiding the development of fast-ion-conducting solid electrolytes. While further experimental validation is necessary, the results offer valuable directions for improving sodium-ion battery systems paired with sodium metal anodes. This combination holds promise for sustainable energy storage solutions in stationary applications or mobile systems with less stringent energy density requirements.

List of symbols

a_s	Specific interfacial surface area, $m^2\,m^{-3}$
A_{cc}	Current collector plate area, m^2
A_c	Total contact area of the domain, m^2
A_f	Contact area between two particles, m^2
c_{el}	Electrolyte sodium ion concentration, $mol\,m^{-3}$
c_s	Active material sodium ion concentration, $mol\,m^{-3}$
C	C-rate, h^{-1}
C_f	Shape factor
d	Space dimension
D_{el}	Electrolyte sodium ion diffusion coefficient, $m^2\,s^{-1}$
D_s	Active material sodium diffusion coefficient , $m^2\,s^{-1}$
F	Faraday constant, $C\,mol^{-1}$
i_0	Exchange current density, $A\,m^{-2}$
$\boldsymbol{i}_{cell}$	Total cell current density, $A\,m^{-2}$
$\boldsymbol{i}_{el}$	Electrolyte current density, $A\,m^{-2}$
$\boldsymbol{i}_s$	Active material current density, $A\,m^{-2}$
j_{BV}	Butler–Volmer flux density, $mol\,m^{-2}\,s^{-1}$
k	Butler–Volmer reaction constant, $m^{2.5}\,mol^{-0.5}\,s^{-1}$
k_c	Reduced core ionic conductivity in the ZBS model
k_P	Ratio of ionic conductivities of dispersed and continuous phase in the ZBS model
L_{pos}	Length of the positive half cell, m
L_{sep}	Length of the separator, m
N_P	Number of particles
R	Universal gas constant, $J\,mol^{-1}\,K^{-1}$
R_{AM}	Active material particle radius, m
t_+^0	Transference number of sodium ions in the electrolyte
U_{eq}	Equilibrium potential, V
q	Physical quantity
b_{Brug}	Bruggeman's exponent
γ	Flattening coefficient
ε_{el}	Electrolyte porosity
ε_s	Active material porosity
κ	Electrolyte ionic conductivity, $S\,m^{-1}$
κ_d	Electrolyte diffusional conductivity, $S\,m^{-1}$
κ_{fil}	Active filler ionic conductivity, $S\,m^{-1}$
κ_{pol}	Polymer ionic conductivity, $S\,m^{-1}$
σ	Active material conductivity, $S\,m^{-1}$
τ	Electrode tortuosity
$\boldsymbol{\Phi}_{el}$	Electrolyte potential, V
$\boldsymbol{\Phi}_s$	Active material potential, V
φ_{AM}	Active material content
φ_{fil}	Active filler volume fraction
φ_{pol}	Polymer volume fraction
$\varphi_{el,fil}$	Electrolyte active filler volume fraction
$\varphi_{el,pol}$	Electrolyte polymer volume fraction
χ	Mole fraction, $mol\,mol^{-1}$

CRediT authorship contribution statement

F. Gerbig: Writing – review & editing, Writing – original draft, Visualization, Validation, Software, Methodology, Investigation, Formal analysis, Data curation, Conceptualization. **J. Kühn:** Visualization, Software, Investigation, Data curation. **H. Nirschl:** Writing – review & editing, Resources, Project administration.

Declaration of Generative AI and AI-assisted technologies in the writing process

During the preparation of this work the authors used OpenAI's ChatGPT, based on the GPT-3.5 architecture in order to assist in the grammar and language review of this manuscript. After using this tool, the authors reviewed and edited the content as needed and take full responsibility for the content of the publication.

Declaration of competing interest

The authors declare that they have no known competing financial interests or personal relationships that could have appeared to influence the work reported in this paper.

Acknowledgment

The authors acknowledge funding and support from the German Federal Ministry of Education and Research (Bundesministerium für Bildung und Forschung) under project number 03XP0403D. The responsibility for the content is with the authors. Additionally, this research received support from the state of Baden-Württemberg through bwHPC.

Data availability

Data will be made available on request.

References

Andersson, J.A.E., Gillis, J., Horn, G., Rawlings, J.B., Diehl, M., 2019. CasADi: a software framework for nonlinear optimization and optimal control. Math. Program. Comput. 11 (1), 1–36. http://dx.doi.org/10.1007/s12532-018-0139-4.

Åvall, G., Mindemark, J., Brandell, D., Johansson, P., 2018. Sodium–Ion battery electrolytes: Modeling and simulations. Adv. Energy Mater. 8 (17), 1703036. http://dx.doi.org/10.1002/aenm.201703036.

Bazant, M.Z., 2023. Unified quantum theory of electrochemical kinetics by coupled ion-electron transfer. Faraday Discuss. 246, 60–124. http://dx.doi.org/10.1039/d3fd00108c.

Blumberg, W., Schlünder, E.-U., 1995. Thermal conductivity of packed beds consisting of porous particles wetted with binary mixtures. Chem. Eng. Process.: Process Intensif. 34 (3), 339–346. http://dx.doi.org/10.1016/0255-2701(95)00583-8.

Brosa Planella, F., Ai, W., Boyce, A.M., Ghosh, A., Korotkin, I., Sahu, S., Sulzer, V., Timms, R., Tranter, T.G., Zyskin, M., Cooper, S.J., Edge, J.S., Foster, J.M., Marinescu, M., Wu, B., Richardson, G., 2022. A continuum of physics-based lithium-ion battery models reviewed. Prog. Energy 4 (4), 042003. http://dx.doi.org/10.1088/2516-1083/ac7d31.

Bruggeman, D.A.G., 1935. Berechnung verschiedener physikalischer konstanten von heterogenen substanzen. I. Dielektrizitätskonstanten und leitfähigkeiten der mischkörper aus isotropen substanzen. Ann. Phys., Lpz. 416 (7), 636–664. http://dx.doi.org/10.1002/andp.19354160705.

Cernak, S., Gerbig, F., Kespe, M., Nirschl, H., 2020. Spatially resolved lithium–ion battery simulations of the influence of lithium–nickel–manganese–cobalt–oxide particle roughness on the electrochemical performance. Energy Storage 2 (5), e156. http://dx.doi.org/10.1002/est2.156.

Chayambuka, K., Mulder, G., Danilov, D.L., Notten, P.H., 2022. Physics-based modeling of sodium-ion batteries part II. Model and validation. Electrochim. Acta 404, 139764. http://dx.doi.org/10.1016/j.electacta.2021.139764.

Chen, M., Hua, W., Xiao, J., Cortie, D., Chen, W., Wang, E., Hu, Z., Gu, Q., Wang, X., Indris, S., Chou, S.-L., Dou, S.-X., 2019. NASICON-type air-stable and all-climate cathode for sodium-ion batteries with low cost and high-power density. Nat. Commun. 10 (1), 1480. http://dx.doi.org/10.1038/s41467-019-09170-5.

Chen, G., Huang, Q., Wu, T., Lu, L., 2020. Polyanion sodium vanadium phosphate for next generation of Sodium–Ion batteries—A review. Adv. Funct. Mater. 30 (34), 2001289. http://dx.doi.org/10.1002/adfm.202001289.

Chun, J., Wang, X., Zhang, Y., Wei, C., Wang, Z., Feng, J., 2023. Ti3C2Tx film current collectors for high-performance sodium-ion batteries. Vacuum 207, 111476. http://dx.doi.org/10.1016/j.vacuum.2022.111476.

Darjazi, H., Falco, M., Colò, F., Balducci, L., Piana, G., Bella, F., Meligrana, G., Nobili, F., Elia, G.A., Gerbaldi, C., 2024. Electrolytes for sodium ion batteries: The current transition from liquid to solid and hybrid systems. Adv. Mater. (Deerfield Beach, Fla.) 36 (35), e2313572. http://dx.doi.org/10.1002/adma.202313572.

Delmas, C., 2018. Sodium and sodium-ion batteries: 50 years of research // sodium and sodium–Ion batteries: 50 years of research. Adv. Energy Mater. 8 (17), 1703137. http://dx.doi.org/10.1002/aenm.201703137.

Dong, Y., Wen, P., Shi, H., Yu, Y., Wu, Z.-S., 2024. Solid–state electrolytes for sodium metal batteries: Recent status and future opportunities. Adv. Funct. Mater. 34 (5), 2213584. http://dx.doi.org/10.1002/adfm.202213584.

Doyle, M., Fuller, T.F., Newman, J., 1993. Modeling of galvanostatic charge and discharge of the Lithium/Polymer/Insertion Cell. J. Electrochem. Soc. 140 (6), 1526–1533. http://dx.doi.org/10.1149/1.2221597.

Eshetu, G.G., Elia, G.A., Armand, M., Forsyth, M., Komaba, S., Rojo, T., Passerini, S., 2020. Electrolytes and interphases in sodium–based rechargeable batteries: Recent advances and perspectives. Adv. Energy Mater. 10 (20), 2000093. http://dx.doi.org/10.1002/aenm.202000093.

Fan, L., Li, X., 2018. Recent advances in effective protection of sodium metal anode. Nano Energy 53, 630–642. http://dx.doi.org/10.1016/j.nanoen.2018.09.017.

Fuentes, R.O., Marques, F.M.B., Franco, J.I., 1999. Síntesis y propiedades de Nasicon preparado a partir de diferentes precursores basados en circonia. Bol. Soc. Española Cerám. Vidrio 38 (6), 631–634. http://dx.doi.org/10.3989/cyv.1999.v38.i6.908.

Gao, H., Xue, L., Xin, S., Park, K., Goodenough, J.B., 2017. A plastic-crystal electrolyte interphase for all-solid-state sodium batteries. Angew. Chem. (Int. ed. Engl.) 56 (20), 5541–5545. http://dx.doi.org/10.1002/anie.201702003.

Garapati, V.K., Dingari, N.N., Mynam, M., Rai, B., 2023. Physics-based reduced order model for sodium-ion batteries. J. Electrochem. Soc. 170 (1), 010517. http://dx.doi.org/10.1149/1945-7111/acb01b.

Gerbig, F., Chauhan, A., Gietl, S., Nirschl, H., 2024. Performance investigations on all-solid-state polymer-ceramic sodium-ion batteries through a spatially resolved electrochemical model. J. Electrochem. Soc. 171 (9), 090515. http://dx.doi.org/10.1149/1945-7111/ad7763.

Goldin, G.M., Colclasure, A.M., Wiedemann, A.H., Kee, R.J., 2012. Three-dimensional particle-resolved models of Li-ion batteries to assist the evaluation of empirical parameters in one-dimensional models. Electrochim. Acta 64, 118–129. http://dx.doi.org/10.1016/j.electacta.2011.12.119.

Haimes, Y.Y., 1973. Integrated System Identification and Optimization. In: Control and Dynamic Systems, Vol. 10, Academic Press, pp. 435–518. http://dx.doi.org/10.1016/B978-0-12-012710-8.50013-3.

Jamnik, J., Kalnin, J.R., Kotomin, E.A., Maier, J., 2006. Generalised Maxwell-Garnett equation: application to electrical and chemical transport. Phys. Chem. Chem. Phys. : PCCP 8 (11), 1310–1314. http://dx.doi.org/10.1039/b514448p.

Jin, T., Li, H., Zhu, K., Wang, P.-F., Liu, P., Jiao, L., 2020. Polyanion-type cathode materials for sodium-ion batteries. Chem. Soc. Rev. 49 (8), 2342–2377. http://dx.doi.org/10.1039/c9cs00846b.

Kaus, M., Guin, M., Yavuz, M., Knapp, M., Tietz, F., Guillon, O., Ehrenberg, H., Indris, S., 2017. Fast Na + Ion conduction in NASICON-type Na 3.4 Sc 2 (SiO 4) 0.4 (PO 4) 2.6 observed by 23 Na NMR relaxometry. J. Phys. Chem. C 121 (3), 1449–1454. http://dx.doi.org/10.1021/acs.jpcc.6b10523.

Kim, E.J., Kumar, P.R., Gossage, Z.T., Kubota, K., Hosaka, T., Tatara, R., Komaba, S., 2022. Active material and interphase structures governing performance in sodium and potassium ion batteries. Chem. Sci. 13 (21), 6121–6158. http://dx.doi.org/10.1039/d2sc00946c.

Li, C., Xu, H., Ni, L., Qin, B., Ma, Y., Jiang, H., Xu, G., Zhao, J., Cui, G., 2023. Nonaqueous liquid electrolytes for Sodium–Ion Batteries: Fundamentals, progress and perspectives. Adv. Energy Mater. 13 (40), 2301758. http://dx.doi.org/10.1002/aenm.202301758.

Liu, X., Feng, G., Wang, E., Chen, H., Wu, Z., Xiang, W., Zhong, Y., Chen, Y., Guo, X., Zhong, B., 2019. Insight into preparation of Fe-Doped Na3V2(PO4)3@C from aspects of particle morphology design, crystal structure modulation, and carbon graphitization regulation. ACS Appl. Mater. Interfaces 11 (13), 12421–12430. http://dx.doi.org/10.1021/acsami.8b21257.

Liu, Y., Li, J., Shen, Q., Zhang, J., He, P., Qu, X., Liu, Y., 2022. Advanced characterizations and measurements for sodium-ion batteries with NASICON-type cathode materials. eScience 2 (1), 10–31. http://dx.doi.org/10.1016/j.esci.2021.12.008.

Liu, Q., Zhao, X., Yang, Q., Hou, L., Mu, D., Tan, G., Li, L., Chen, R., Wu, F., 2023. The progress in the electrolytes for solid state Sodium–Ion battery. Adv. Mater. Technol. 8 (7), 2200822. http://dx.doi.org/10.1002/admt.202200822.

Mongcopa, K.I.S., Tyagi, M., Mailoa, J.P., Samsonidze, G., Kozinsky, B., Mullin, S.A., Gribble, D.A., Watanabe, H., Balsara, N.P., 2018. Relationship between segmental dynamics measured by quasi-elastic neutron scattering and conductivity in polymer electrolytes. ACS Macro Lett. 7 (4), 504–508. http://dx.doi.org/10.1021/acsmacrolett.8b00159.

Moradipour, F., Markert, A., Rudszuck, T., Röttgen, N., Dück, G., Finsterbusch, M., Gerbig, F., Nirschl, H., Guthausen, G., 2023. Na^+ Mobility in PEO-based composite solid-state electrolytes by NMR. J. Energy Power Technol. 05 (04), 1–21. http://dx.doi.org/10.21926/jept.2304032.

Nayak, P.K., Yang, L., Brehm, W., Adelhelm, P., 2018. From lithium-ion to sodium-ion batteries: Advantages, challenges, and surprises. Angew. Chem. (Int. ed. Engl.) 57 (1), 102–120. http://dx.doi.org/10.1002/anie.201703772.

Newman, J., Balsara, N.P., 2021. Electrochemical Systems, fourth ed. In: The Electrochemical Society Series, Wiley, Hoboken, NJ.

Novikova, S.A., Larkovich, R.V., Chekannikov, A.A., Kulova, T.L., Skundin, A.M., Yaroslavtsev, A.B., 2018. Electrical conductivity and electrochemical characteristics of Na3V2(PO4)3-based NASICON-type materials. Inorg. Mater. 54 (8), 794–804. http://dx.doi.org/10.1134/S0020168518080149.

Plett, G.L., 2015. Battery Management Systems: Volume 1: Battery Modeling. Artech House Power Engineering and Power Electronics, Vol. 1, Artech House, Boston.

Przyluski, J., Siekierski, M., Wieczorek, W., 1995. Effective medium theory in studies of conductivity of composite polymeric electrolytes. Electrochim. Acta 40 (13–14), 2101–2108. http://dx.doi.org/10.1016/0013-4686(95)00147-7.

Rodrigues, S.J., Vorhauer-Huget, N., Tsotsas, E., 2023. Prediction of effective thermal conductivity of packed beds of polyhedral particles. Powder Technol. 430, 118997. http://dx.doi.org/10.1016/j.powtec.2023.118997.

Serra Moreno, J., Armand, M., Berman, M.B., Greenbaum, S.G., Scrosati, B., Panero, S., 2014. Composite PEOn:NaTFSI polymer electrolyte: Preparation, thermal and electrochemical characterization. J. Power Sources 248, 695–702. http://dx.doi.org/10.1016/j.jpowsour.2013.09.137.

Shen, L., Chen, Z., 2007. Critical review of the impact of tortuosity on diffusion. Chem. Eng. Sci. 62 (14), 3748–3755. http://dx.doi.org/10.1016/j.ces.2007.03.041.

Si, L., Yuan, Z., Hu, L., Zhu, Y., Qian, Y., 2014. Uniform and continuous carbon coated sodium vanadium phosphate cathode materials for sodium-ion battery. J. Power Sources 272, 880–885. http://dx.doi.org/10.1016/j.jpowsour.2014.09.046.

Storn, R., Price, K., 1997. Differential evolution – A simple and efficient heuristic for global optimization over continuous spaces. J. Global Optim. 11 (4), 341–359. http://dx.doi.org/10.1023/A:1008202821328.

Sulzer, V., Marquis, S.G., Timms, R., Robinson, M., Chapman, S.J., 2021. Python battery mathematical modelling (PyBaMM). J. Open Res. Softw. 9 (1), 14. http://dx.doi.org/10.5334/jors.309.

Teran, A.A., Balsara, N.P., 2014. Thermodynamics of block copolymers with and without salt. J. Phys. Chem. B 118 (1), 4–17. http://dx.doi.org/10.1021/jp408079z.

Thomas, K.E., Newman, J., Darling, R.M., 2002. Mathematical modeling of lithium batteries. In: van Schalkwijk, W.A., Scorsati, B. (Eds.), Advances in Lithium-Ion Batteries. Kluwer Academic/Plenum Publ, New York, pp. 345–392. http://dx.doi.org/10.1007/0-306-47508-1{_}13.

Titirici, M.-M., Adelhelm, P., Hu, Y.-S. (Eds.), 2022. Sodium–Ion Batteries: Materials, Characterization, and Technology. Wiley, Weinheim, http://dx.doi.org/10.1002/9783527825769.

Tsotsas, E., Martin, H., 1987. Thermal conductivity of packed beds: A review. Chem. Eng. Process.: Process Intensif. 22 (1), 19–37. http://dx.doi.org/10.1016/0255-2701(87)80025-9.

Usiskin, R., Lu, Y., Popovic, J., Law, M., Balaya, P., Hu, Y.-S., Maier, J., 2021. Fundamentals, status and promise of sodium-based batteries. Nat. Rev. Mater. 6 (11), 1020–1035. http://dx.doi.org/10.1038/s41578-021-00324-w.

Wróbel, P., Kubisiak, P., Eilmes, A., 2021. NaFSI and NaTFSI solutions in Ether solvents from Monoglyme to Poly(ethylene oxide)-A molecular dynamics study. J. Phys. Chem. B 125 (36), 10293–10303. http://dx.doi.org/10.1021/acs.jpcb.1c05793.

Yim, C.-H., Houache, M.S., Baranova, E.A., Abu-Lebdeh, Y., 2023. Understanding key limiting factors for the development of all-solid-state-batteries. Chem. Eng. J. Adv. 13, 100436. http://dx.doi.org/10.1016/j.ceja.2022.100436.

Zeng, J., Yang, Y., Lai, S., Huang, J., Zhang, Y., Wang, J., Zhao, J., 2017. A promising high-voltage cathode material based on mesoporous Na3 V2 (PO4)3 /C for rechargeable magnesium batteries. Chem. (Weinheim Bergstrasse Ger.) 23 (66), 16898–16905. http://dx.doi.org/10.1002/chem.201704303.

Zhang, Z., Zhang, Q., Ren, C., Luo, F., Ma, Q., Hu, Y.-S., Zhou, Z., Li, H., Huang, X., Chen, L., 2016. A ceramic/polymer composite solid electrolyte for sodium batteries. J. Mater. Chem. A 4 (41), 15823–15828. http://dx.doi.org/10.1039/C6TA07590H.

Zheng, Q., Yi, H., Liu, W., Li, X., Zhang, H., 2017. Improving the electrochemical performance of Na 3 V 2 (PO 4) 3 cathode in sodium ion batteries through Ce/V substitution based on rational design and synthesis optimization. Electrochim. Acta 238, 288–297. http://dx.doi.org/10.1016/j.electacta.2017.04.029.

Zou, Z., Li, Y., Lu, Z., Da Wang, Cui, Y., Guo, B., Li, Y., Liang, X., Feng, J., Li, H., Nan, C.-W., Armand, M., Chen, L., Xu, K., Shi, S., 2020. Mobile ions in composite solids. Chem. Rev. 120 (9), 4169–4221. http://dx.doi.org/10.1021/acs.chemrev.9b00760.